Contrast enhancement in near-infrared electro-optic imaging

MIKHAIL MAMAIKIN,[1,2] ENRICO RIDENTE,[1,2,3] NAJD ALTWAIJRY,[1,2] MATTHEW WEIDMAN,[1,2] AND NICHOLAS KARPOWICZ[1,4,*]

[1]*Max-Planck-Institut für Quantenoptik, Hans-Kopfermann-Strasse 1, 85748 Garching, Germany*
[2]*Fakultät für Physik, Ludwig-Maximilians-Universität, Am Coulombwall 1, 85748 Garching, Germany*
[3]*Currently with Department of Chemistry, University of California, Berkeley, CA, USA*
[4]*CNR NANOTEC Institute of Nanotechnology, via Monteroni, 73100 Lecce, Italy*
[*]*nicholas.karpowicz@mpq.mpg.de*

Abstract: Access to subtle ultrafast effects of light-matter interaction often requires highly sensitive field detection schemes. Electro-optic sampling, being an exemplary technique in this regard, lacks high sensitivity in an imaging geometry. We demonstrate a straightforward method to significantly improve the contrast of electric field images in spatially resolved electro-optic sampling. A thin-film polarizer is shown to be an effective tool in enhancing the sensitivity of the electro-optic imaging system, enabling an adjustment of the spectral response. We show a further increase of the signal-to-noise ratio through the direct control of the carrier envelope phase of the imaged field.

1. Introduction

The ability to measure and control electric fields of few-cycle laser pulses, including the carrier envelope phase (CEP), has introduced new directions to track the ultrafast response of matter on a sub-cycle time scale [1–3]. Highly nonlinear techniques [4–6] like attosecond streaking have been applied in the near-infrared and visible spectral regions to extract comprehensive information about light-matter interaction, such as energy transfer in solids [7] and photoionization dynamics in liquids [8], requiring a vacuum environment and an intense laser pulse to produce extreme ultraviolet attosecond bursts. The complexity and cost of these techniques drove the development of simple table-top metrology approaches [9,10]. Free-space electro-optic sampling (EOS), introduced in the terahertz [11,12], is particularly attractive due to its high dynamic range and sensitivity to very weak light fields [13,14]. Recently, it has been shown that EOS can be extended to operate in the near infrared [15] and visible [16], covering the spectral ranges of the majority of the laser sources.

Apart from the pure time-domain studies, EOS has been extended to the spatial domain, yielding the electric field in the form of a two-dimensional image for each time instant [17,18]. EOS imaging maps the electric field in both time and space providing absolute spatio-temporal information about a pulse under study, including the CEP at each point of the cross section [19,20]. The technique can be used to directly probe a complex spatio-temporal response of matter excited with structured light fields or perform near-field studies of optically active devices such as plasmonic and photonic structures deposited directly on the nonlinear crystal [21–23]. EOS imaging provides simultaneous sub-cycle temporal and sub-wavelength spatial resolution with wide field imaging capability, avoiding long probe raster scanning [24,25]. Its application in biology and medicine is highly promising for the real time observations of the morphological changes of various bio samples on the nanometer scale.

Recently, we have applied EOS imaging to characterize few-cycle waveforms with a complex spatial structure in the near-infrared spectral range [26]. For such rapidly oscillating (over 200 THz) and broadband electric fields, EOS requires the use of birefringent crystals with exceptional

group-velocity matching characteristics like beta-barium borate (BBO), which has a relatively low nonlinear coefficient. For near-field measurements, it is also necessary to use thin crystals to capture near-field and evanescent radiation [26–28]. Imaging imposes the additional requirement of a large acceptance angle of the nonlinear process, as one wishes to record the electric field over a large range of wave vectors. These conditions pose several technical challenges that complicate the recording of a field image with high signal-to-noise ratio (SNR). In particular, a thin crystal limits the contrast of the EOS image, which is contained in the difference between two captured images, making difficult to extract the field image in the presence of shot noise. In this paper, we describe two approaches that significantly improve the SNR of extracted field images, enabling an adjustment of the EOS response to the frequency region of interest.

2. Concept and experimental setup

EOS is the encoding of the test electric field into a rotation of the polarization state of an ultrashort probe pulse in a second-order nonlinear crystal (EOS crystal) via the Pockels effect. By changing the relative time delay between the two pulses, it is possible to record the time-varying polarization rotation and fully reconstruct the sampled field. When rapidly-oscillating test fields are considered, it is useful to describe EOS in terms of heterodyne detection, where a pulse generated via sum (or difference) frequency generation, is a spectrally up-shifted (or down-shifted) orthogonally polarized replica of the probe pulse [29]. To produce a polarization rotation, this nonlinear wave must interfere on the detector with the reference frequencies contained in the original probe spectrum, which serve as a local oscillator (LO) in the detection [30,31]. By spectrally filtering the overlap region it is possible to shift the detection limits of EOS towards shorter wavelengths and significantly suppress the noise [15,24,32,33].

When using balanced photodiodes, time-domain EOS averages the spatial dependence of the polarization rotation and, thus, requires an assumption of spatial uniformity of the test electric field. In contrast, EOS imaging records the complete electric field structure in both time and space as a series of snapshots. This can be achieved through a simple imaging system using an objective lens, a camera, and the balanced detection [34]. The camera, however, provides a lower dynamic range compared to the balanced photodiodes, without a possibility to use a lock-in amplifier to additionally suppress the noise [28].

Our EOS imaging system investigates a 15 fs infrared (IR) waveform centered at 2 μm using a 0.5–1 μm white-light probe pulse (Fig. 1(a)) [35]. The IR field is produced via intra-pulse difference frequency generation (DFG) of the white-light pulse, passively stabilizing the CEP of the generated waveform. The spectral phase of the IR pulse is shaped using an acousto-optic programmable dispersive filter (AOPDF, Fastlite DAZZLER), enabling the direct control of the CEP. After optical parametric chirped pulse amplification (OPCPA), 30 nJ of the IR pulse energy is recombined with the residual 4 fs white-light pulse (4 μJ) using a broadband wire-grid polarizer (WGP). The IR and probe beams are subsequently focused into a 100-μm-thick type-II BBO for sum frequency generation (SFG) using a BaF$_2$ lens (FL = 100 mm) and an adjustable telescope, respectively. The cross-section of the probe is enlarged ($\sim$ 300 μm at 1/e^2) with respect to the IR beam ($\sim$ 100 μm at 1/e^2) to fully resolve the spatial structure of the latter.

The nonlinearly generated wave in the BBO at an instant of the time delay τ is proportional to the input IR and probe electric fields, $E_{SFG}(\omega) \propto C_{NL}\exp(i\Omega\tau)E_{IR}(\Omega)E_p(\omega - \Omega)$, where ω and Ω are frequencies of the SFG and IR field, respectively, and C_{NL} is a constant determined by the EOS crystal. The BBO is imaged by a 4x microscope objective (NA = 0.1) and a pair of tube lenses (FL = 175 mm) onto a CCD camera (Cinogy CinCam CCD-2302-UV, with a 3.45 μm pixel size). After the projection of $E_{LO} = E_p(\omega)$ and $E_{SFG}(\omega)$ onto one another by a WGP tilted at 45°, the resulting reflected (R) and transmitted (T) through the WGP beams produce two orthogonally polarized images on different parts of the active area of CCD. These images are a result of the
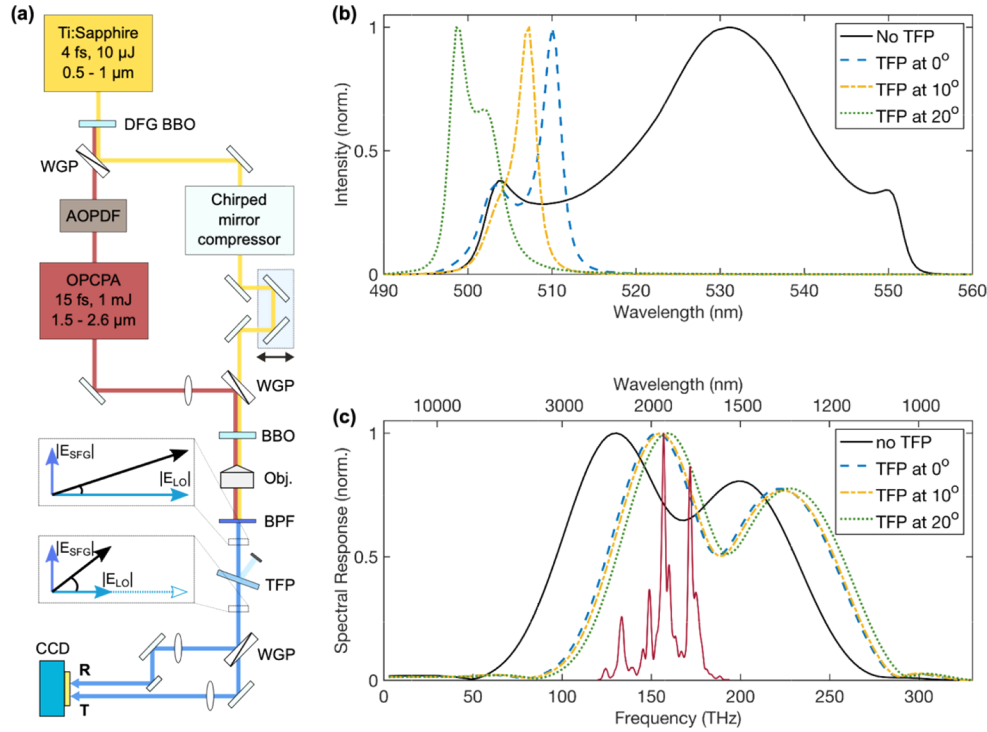
Fig. 1. Experimental layout and EOS spectral response control using the TFP. (a) Spectrally broadened Ti:Sapphire laser pulses are utilized to generate the phase-stable IR waveform in BBO through intra-pulse difference frequency generation (DFG). The spectral phase and CEP of the IR pulse is fine-tuned using an acousto-optic programmable dispersive filter (AOPDF). The IR pulse after optical parametric chirped pulse amplification (OPCPA) is recombined with the recompressed white light using a wire-grid polarizer (WGP) for sum frequency generation (SFG) in BBO. The BBO is imaged using a 4x objective lens, a pair of tube lenses and a CCD camera after passing through the band-pass filter (BPF, 500–550 nm). A thin-film polarizer (TFP, 532 nm) is placed to balance the relative amplitudes of the SFG and LO (see insets) and increase the effective polarization rotation. The reflected (R) and transmitted (T) through the WGP placed at 45° form two cross-polarized images on the CCD to be recorded simultaneously. **(b)** Spectrum of the LO measured without the TFP and at different AOI on the TFP. **(c)** Corresponding spectral response of EOS calculated based on (b), with the spectrum of the input IR pulse (solid red line).

interference of the light pulses that reach the CCD:

$$R \propto |E_{LO} + E_{SFG}|^2 = |E_{LO}|^2 + |E_{SFG}|^2 + 2|E_{LO}||E_{SFG}| \cos \phi, \tag{1}$$

$$T \propto |E_{LO} - E_{SFG}|^2 = |E_{LO}|^2 + |E_{SFG}|^2 - 2|E_{LO}||E_{SFG}| \cos \phi, \tag{2}$$

with $\phi = \Omega\tau + \phi_{IR}(\Omega) + \Delta\phi_p(\omega, \Omega)$, where $\phi_{IR}(\Omega)$ is the phase of the IR field and $\Delta\phi_p(\omega, \Omega)$ is the phase difference between the LO and the probe frequency that mixed with the infrared field during SFG. If the probe pulse is transform-limited, then $\Delta\phi_p = 0$; since it is a relative phase, it does not depend on the carrier-envelope phase of the probe pulse and can be fully characterized by a self-referenced pulse measurement technique such as FROG if one wishes to subtract it from the measured phase. For an extended derivation of the Eqs. (1) and (2) see Supplement 1. The cross terms of the Eqs. (1) and (2) are responsible for the interference and EOS detection. We calculate the EOS signal S, which is proportional to the weak IR field, as

$$E_{IR} \propto S = \tfrac{1}{2} \tfrac{R-T}{R+T}. \tag{3}$$

The normalization used in Eq. (3) reduces the spatial effects of the probe amplitude variations, although the SNR still varies spatially. The signal S has a local maximum when the ratio $|E_{SFG}|/|E_{LO}|$ approaches unity, providing the highest interference strength of the corresponding fields. This condition can be obtained by optimizing the upconversion process, i.e., increasing C_{NL} or $|E_{IR}|$. These are limited by physical constraints, however: the nonlinear coefficient of the crystal and its thickness, the energy of the infrared pulse, or the saturation of the wave-mixing process in the BBO, which defines the maximum input IR pulse energy in our case. Alternatively, a careful control of $|E_{LO}|$ can be used to reduce the number of LO photons as long as the photon flux is sufficient to be measured by the CCD. This can also lower the shot noise level, which scales with the square root of the total intensity incident on the CCD.

A set of carefully aligned Brewster wedges shown in time-domain EOS seems to be a viable approach to decrease the LO amplitude [36]. For an imaging geometry, however, the use of wedged transmissive optics must be avoided, since spatial and chromatic distortions can be introduced. A more advanced realization of the same SNR enhancement principle was implemented in [37,38] where two consequent measurements with opposite sign of small optical bias are required to extract the electric field and remove induced signal distortions. Although high SNR improvement can be achieved in this case, a variable tilt of the WGP can lead to image misalignment in our experimental configuration, additionally doubling time of the data acquisition. As was shown in [39], in the limit of detecting weak fields, these distortions are negligible, and only a single scan is necessary.

Here, we utilize a conventional thin-film polarizer plate (TFP, EKSMA Optics) designed to work around a wavelength of 532 nm. The TFP can effectively control the relative amplitudes between the LO (S-polarization) and SFG (P-polarization) by varying the angle of incidence (AOI) of the input pulses at the TFP. For a detailed analysis of the polarizing properties of the TFP as a function of the AOI, see Supplement 1. Since our TFP provides excessively high extinction ratio (~ 200) at Brewster angle, we balance two orthogonal components by decreasing the AOI. As we will show, this can significantly enhance the interference between the LO and SFG components and, consequently, the relative contrast of the resulting images.

Since in any linear field detection measurement, the measured signal S is the convolution of input test field with the frequency-dependent response function of the detection, an accurate analysis of the response function is necessary to reconstruct the IR field. Similar to our previous

work [15], we define the response function $R(\Omega)$ of EOS as

$$R(\Omega) = \int_\Omega^\infty d\omega \, r(\omega)|E_p(\omega)||E_p(\omega - \Omega)|exp(i\Delta\phi_p(\omega, \Omega)), \tag{4}$$

where $r(\omega)$ is the frequency response of the CCD and the optical system including transmission of the LO through the band-pass filter (BPF) of 500-550 nm. In this regard, it is important to note that a TFP acts as a band-stop filter for the transmitted LO spectrum due to its multilayer structure, and a variation of the AOI is accompanied by a spectral shift of the band-stop window as depicted in Fig. 1(b). Accordingly, the spectral response of EOS shifts towards higher frequencies as the AOI on the TFP increases (Fig. 1(c)). This can be used to improve the overlap of the response function with the input IR spectrum. Although a similar adjustment of the spectral response can be achieved with a combination of standard BPFs, the dependence of transmission of the LO frequencies on the AOI allows for a fine-tuned spectral control of the detected signal. This feature of the TFP can be particularly useful in measuring, for example, excited vibrations of individual molecules [14] or resonances in plasmonic devices [23,26].

3. Results and discussion

We first show how a change of the AOI on the TFP modifies the interference of SFG and LO on the CCD. In Fig. 2, raw CCD frames are depicted at a positive extremum of the IR waveform. The TFP at normal incidence (AOI of 0°) acts as a standard band-stop filter, removing longer wavelengths in the pass band equally for both polarization states. This does not alter the high number of LO photons, maintaining inefficient interference with SFG and poor sensitivity of the imaging system (Fig. 2(a) and (b)). After the subtraction and normalization of the cross-polarized images, the field image (Fig. 2(c)) does not reveal any noticeable structure. Figure 2(d)-(f) represent the case when the AOI on the TFP is increased to 10°. In the narrowband spectral region around the margins of the band-stop window, this provides higher transmission for the SFG photons than the LO photons (see Supplement 1). However, the low extinction ratio of the TFP at this angle leads only to a minor improvement of the contrast. When the AOI is increased to 20°, cross-polarized images (Fig. 2 (g) and (h)) and the normalized subtraction (Fig. 2(i)) reach a nearly optimal contrast as the extinction ratio is increased and SFG photons experience higher transmission in the broader frequency range. Further increase of the AOI leads to an insufficient photon flux of the LO in the analyzed spectral range to be detected by the CCD and a rapid decrease of the sensitivity.

The final images of the IR electric field are obtained using image post-processing, with the parameters described in Supplement 1. The comparison of the field patterns at the highest field strength is depicted in Fig. 3 for the AOI of 0° and 20°. It is clear that the inhomogeneous field distribution in space causes a spatial variation of the SNR. When the TFP does not enhance the contrast (Fig. 3(a)), strong noise can be particularly noticeable at the margins of the field image, where the IR and probe field strengths are significantly lower. Detection of noncentral spatial regions often provides valuable information about the spatio-temporal field structure including various types of aberrations and distortions. The TFP at 20° drastically improves the contrast across the entire image (Fig. 3(b)) yielding a dynamic range over 90 (Fig. 3(c)). This allows for the enhancement of the sensitivity by a factor of ~ 4.9 compared to the measurement with the TFP placed at normal incidence. The dynamic range for each pixel is calculated as the ratio of the IR field value in Fig. 3(a) and 3(b) to the standard deviation of the noise floor measured when the IR beam was blocked. The noise level of the images for both cases is similar due to neutral density filters with different attenuation factors added to avoid saturation of the CCD.

The SNR strongly depends on the experimental conditions and can be significantly improved by increasing integration time or sacrificing spatial resolution. Nevertheless, the obtained value of the dynamic range is comparable to the EOS imaging systems shown in the terahertz [17,34],
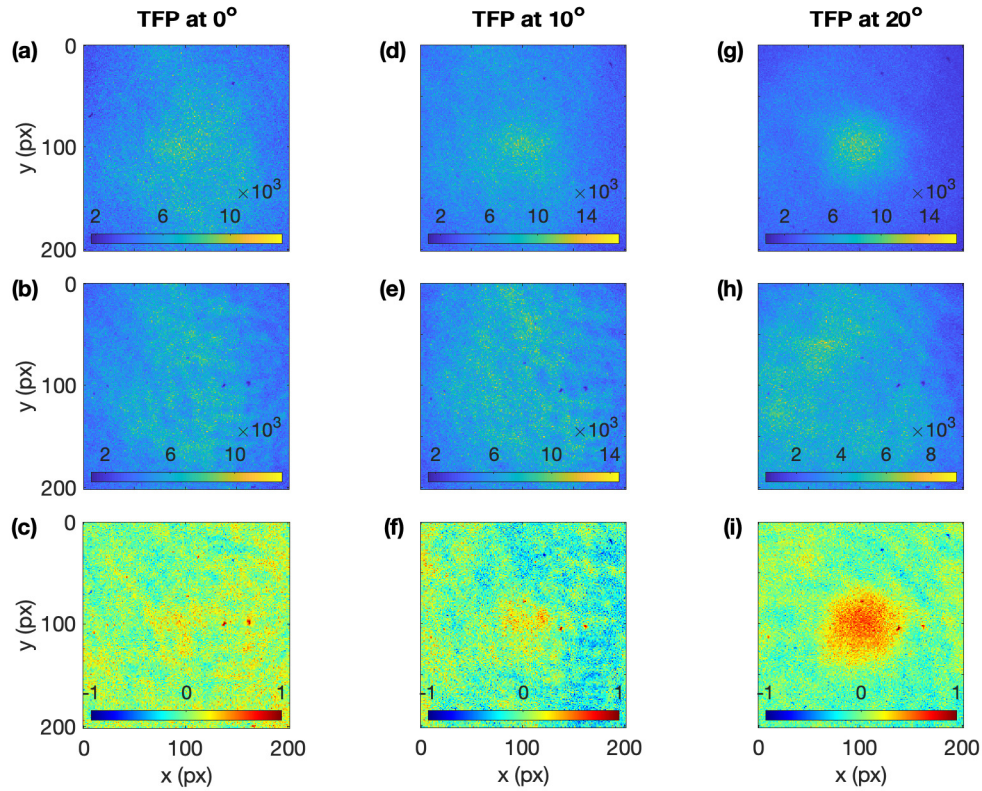
Fig. 2. **CCD frames showing contrast enhancement using the TFP**. Cross-polarized images and the normalized subtraction at the maximum IR field strength produced by the interference of the LO and SFG beams after passing through the TFP at the AOI of **(a)-(c)** 0°, **(d)-(f)** 10° and **(g)-(i)** 20°.

where highly nonlinear detection crystals such as zinc telluride or lithium niobate are widely utilized.

In the last section, we show that the phase modulation utilized, for example, in THz spectroscopy using photoconductive antennas [40], can be also adapted to the EOS imaging system. THz emission from photoconductive antennas is commonly modulated using the direction of the bias voltage, but a similar level of control is difficult to achieve with sources driven by intra-pulse DFG or optical rectification. Here, we modulate the relative CEP of the IR pulse with the AOPDF and apply this to the balanced detection method of acquiring EOS images.

The spatio-temporal information about the electric field with opposite CEP is identical, except for the sign of the field oscillations. Recording two cross-polarized images for both the actual CEP ($CEP_r = 0$) and the CEP changed by π ($CEP_r = \pi$), we acquire four raw cross-polarized images per point of the time delay. The electric field with the $CEP_r = 0$ is depicted in Fig. 4(a), illustrating the spatiotemporal field evolution in the *y-t* domain ($x = 0$) in the case of TFP at 20°. Accordingly, the field structure with $CEP_r = \pi$ shown in Fig. 4(b) has a similar spatio-temporal profile. A direct subtraction of the recorded field patterns with opposite CEP (Fig. 4(c)) allows a factor of 2 increase of the SNR over the use of an optical chopper [28]. This also mitigates technical errors related to geometrical mismatch and spatial misalignment of the two cross-polarized images captured using dynamic subtraction method. Removing artifacts is extremely important in sub-wavelength-scale imaging measurements where a pixel-level precision can be required.
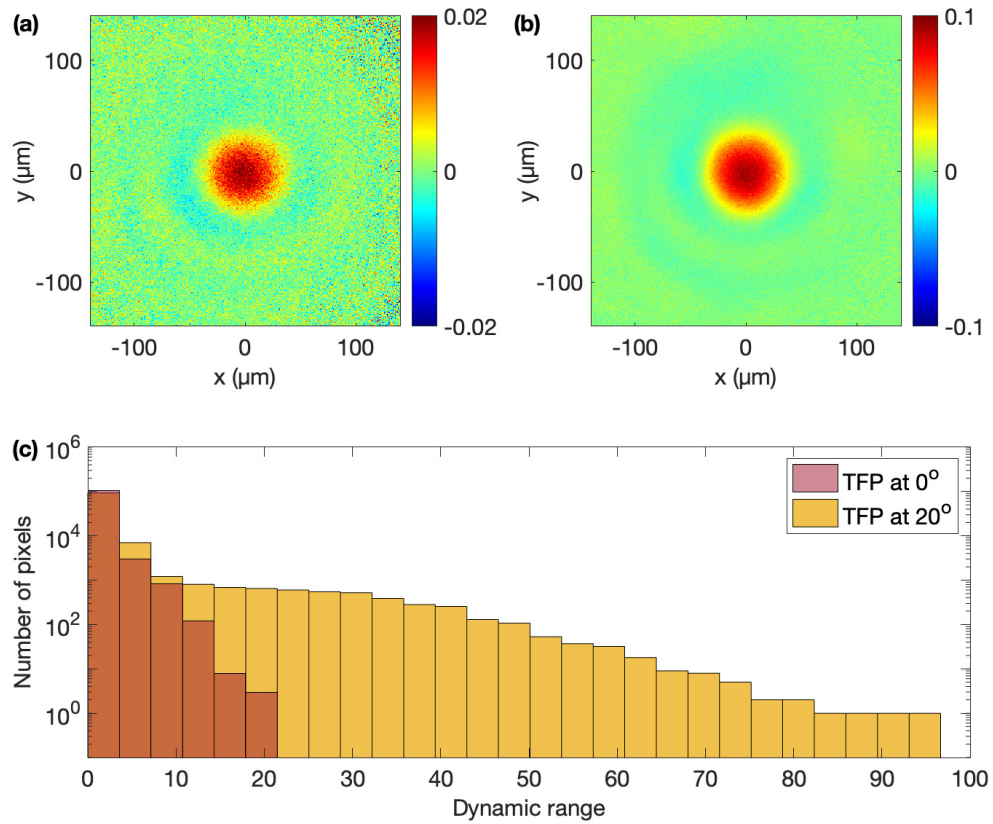
Fig. 3. Contrast comparison of the electric field images. Field structure at the time delay corresponding to the highest field strength obtained using the TFP with the AOI of **(a)** 0° and **(b)** 20°. **(c)** Histogram of the dynamic range calculated for each pixel of the respective images. A sensitivity enhancement factor of ∼ 5 is achieved.
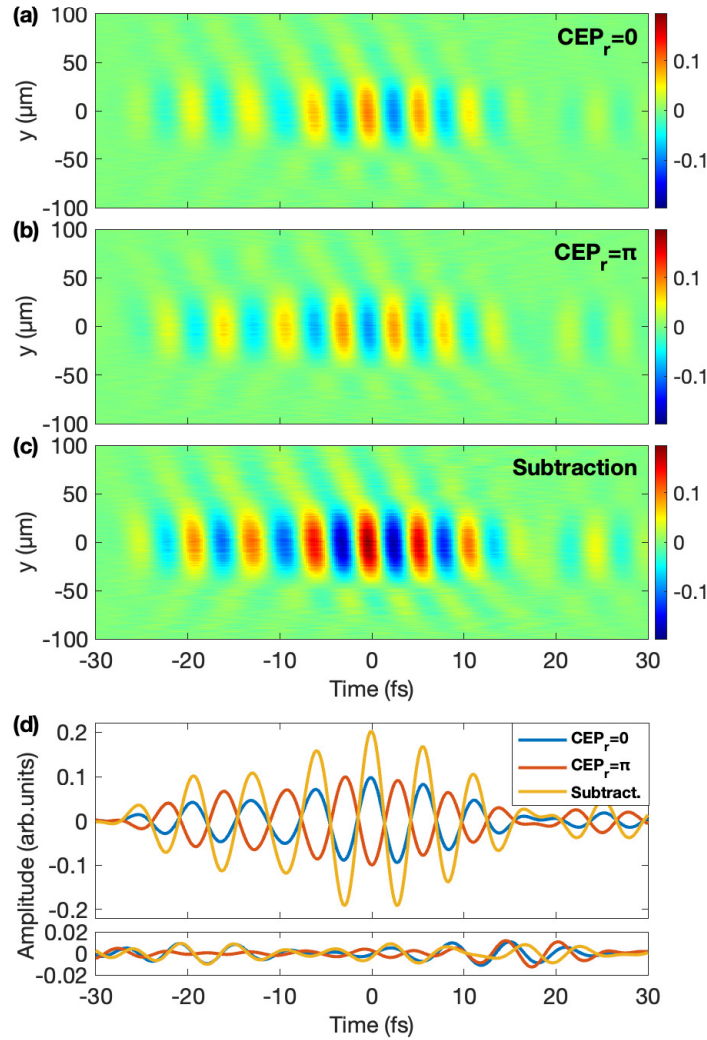
Fig. 4. Carrier envelope phase control for improvement of the signal-to-noise ratio.
Relative CEP control of the IR waveform via the AOPDF can be used to additionally enhance the SNR of EOS images. **(a)** An image of the spatio-temporal electric field with $CEP_r = 0$ in the y-t plane where x = 0 (TFP at 20°). **(b)** A field image captured with $CEP_r = \pi$. **(c)** Direct subtraction of (a) and (b). The images are normalized to the peak amplitude value of (c). **(d)** Time-domain field evolution at x = 0, y = 0, corresponding to the highest field strength for $CEP_r = 0$, $CEP_r = \pi$, and their subtraction. In the plot below, the noise measured for each case with the presence of the IR beam at x = −150 μm, y = −150 μm.

4. Conclusion

In conclusion, we have presented a method to achieve high contrast of near-infrared EOS field images. By adding a cost-effective TFP, the sensitivity of the EOS imaging scheme has been enhanced up to 5 times under our experimental conditions. This facilitates a reliable detection of weak fields in the near infrared and direct observation of the spatio-temporal field dynamics across a wide cross section [27]. The CEP modulation enables an additional improvement of the SNR whenever dynamic control of the phase of the field being measured is available. Both approaches can be directly applied to EOS in a required spectral range. This opens a door for high-sensitive field-resolved microscopy in the molecular fingerprint region, where very small concentrations of various biomolecules can be measured [14].

Disclosures. The authors declare no conflicts of interest.

Data availability. Data underlying the results presented in this paper may be obtained from the authors upon reasonable request.

Supplemental document. See Supplement 1 for supporting content.

References

1. M. Hohenleutner, F. Langer, O. Schubert, M. Knorr, U. Huttner, S. W. Koch, M. Kira, and R. Huber, "Real-time observation of interfering crystal electrons in high-harmonic generation," Nature **523**(7562), 572–575 (2015).
2. W. Kuehn, P. Gaal, K. Reimann, M. Woerner, T. Elsaesser, and R. Hey, "Terahertz induced interband tunneling of electrons in GaAs," Phys. Rev. B **82**(7), 075204 (2010).
3. M. Schultze, E. M. Bothschafter, A. Sommer, S. Holzner, W. Schweinberger, M. Fiess, M. Hofstetter, R. Kienberger, V. Apalkov, V. S. Yakovlev, M. I. Stockman, and F. Krausz, "Controlling dielectrics with the electric field of light," Nature **493**(7430), 75–78 (2013).
4. J. Itatani, F. Quéré, G. L. Yudin, M. Y. Ivanov, F. Krausz, and P. B. Corkum, "Attosecond streak camera," Phys. Rev. Lett. **88**(17), 173903 (2002).
5. K. T. Kim, C. Zhang, A. D. Shiner, B. E. Schmidt, F. Légaré, D. M. Villeneuve, and P. B. Corkum, "Petahertz optical oscilloscope," Nature Photon. **7**(12), 958–962 (2013).
6. A. S. Wyatt, T. Witting, A. Schiavi, D. Fabris, P. Matia-Hernando, I. A. Walmsley, J. P. Marangos, and J. W. G. Tisch, "Attosecond sampling of arbitrary optical waveforms," Optica **3**(3), 303–310 (2016).
7. A. Sommer, E. M. Bothschafter, S. A. Sato, C. Jakubeit, T. Latka, O. Razskazovskaya, H. Fattahi, M. Jobst, W. Schweinberger, V. Shirvanyan, V. S. Yakovlev, R. Kienberger, K. Yabana, N. Karpowicz, M. Schultze, and F. Krausz, "Attosecond nonlinear polarization and light-matter energy transfer in solids," Nature **534**(7605), 86–90 (2016).
8. I. Jordan, M. Huppert, D. Rattenbacher, M. Peper, D. Jelovina, C. Perry, A. von Conta, A. Schild, and H. J. Wörner, "Attosecond spectroscopy of liquid water," Science **369**(6506), 974–979 (2020).
9. S. Sederberg, D. Zimin, S. Keiber, F. Siegrist, M. S. Wismer, V. S. Yakovlev, I. Floss, C. Lemell, J. Burgdörfer, M. Schultze, F. Krausz, and N. Karpowicz, "Attosecond optoelectronic field measurement in solids," Nat. Commun. **11**, 430 (2020).
10. D. Zimin, M. Weidman, J. Schötz, M. F. Kling, V. S. Yakovlev, F. Krausz, and N. Karpowicz, "Petahertz-scale nonlinear photoconductive sampling in air," Optica **8**(5), 586–590 (2021).
11. J. A. Valdmanis, G. Mourou, and C. W. Gabel, "Picosecond electro-optic sampling system," Appl. Phys. Lett. **41**(3), 211–212 (1982).
12. Q. Wu and X.-C. Zhang, "Free-space electro-optic sampling of terahertz beams," Appl. Phys. Lett. **67**(24), 3523–3525 (1995).
13. C. Riek, D. V. Seletskiy, A. S. Moskalenko, J. F. Schmidt, P. Krauspe, S. Eckart, S. Eggert, G. Burkard, and A. Leitenstorfer, "Direct sampling of electric-field vacuum fluctuations," Science **350**(6259), 420–423 (2015).
14. I. Pupeza, M. Huber, M. Trubetskov, W. Schweinberger, S. A. Hussain, C. Hofer, K. Fritsch, M. Poetzlberger, L. Vamos, E. Fill, T. Amotchkina, K. V. Kepesidis, A. Apolonski, N. Karpowicz, V. Pervak, O. Pronin, F. Fleischmann, A. Azzeer, M. Žigman, and F. Krausz, "Field-resolved infrared spectroscopy of biological systems," Nature **577**(7788), 52–59 (2020).
15. S. Keiber, S. Sederberg, A. Schwarz, M. Trubetskov, V. Pervak, F. Krausz, and N. Karpowicz, "Electro-optic sampling of near-infrared waveforms," Nat. Photonics **10**(3), 159–162 (2016).
16. E. Ridente, M. Mamaikin, N. Altwaijry, D. Zimin, M.F. Kling, V. Pervak, M. Weidman, F. Krausz, and N. Karpowicz, "Electro-optic characterization of synthesized infrared-visible light fields," Nat. Commun. **13**, 1111 (2022).
17. Q. Wu, T. D. Hewitt, and X.-C. Zhang, "Two-dimensional electro-optic imaging of THz beams," Appl. Phys. Lett. **69**(8), 1026–1028 (1996).

18. S. Hunsche, M. Koch, I. Brener, and M. C. Nuss, "THz near-field imaging," Opt. Commun. **150**(1-6), 22–26 (1998).
19. J. He, X. Wang, D. Hu, J. Ye, S. Feng, Q. Kan, and Y. Zhang, "Generation and evolution of the terahertz vortex beam," Opt. Express **21**(17), 20230–20239 (2013).
20. M. Takai, M. Takeda, M. Sasaki, T. Tachizaki, N. Yasumatsu, and S. Watanabe, "Video-rate terahertz electric-field vector imaging," Appl. Phys. Lett. **105**(15), 151103 (2014).
21. H. T. Chen, R. Kersting, and G. C. Cho, "Terahertz imaging with nanometer resolution," Appl. Phys. Lett. **83**(15), 3009–3011 (2003).
22. A. Bitzer, H. Merbold, A. Thoman, T. Feurer, H. Helm, and M. Walther, "Terahertz near-field imaging of electric and magnetic resonances of a planar metamaterial," Opt. Express **17**(5), 3826–3834 (2009).
23. T. Arikawa, T. Hiraoka, S. Morimoto, F. Blanchard, S. Tani, T. Tanaka, K. Sakai, H. Kitajima, K. Sasaki, and K. Tanaka, "Transfer of orbital angular momentum of light to plasmonic excitations in metamaterials," Sci. Adv. **6**(24), eaay1977 (2020).
24. F. Blanchard and K. Tanaka, "Improving time and space resolution in electro-optic sampling for near-field terahertz imaging," Opt. Lett. **41**(20), 4645–4648 (2016).
25. F. Blanchard, A. Doi, T. Tanaka, H. Hirori, H. Tanaka, Y. Kadoya, and K. Tanaka, "Real-time terahertz near-eld microscope," Opt. Express **19**(9), 8277–8284 (2011).
26. M. Mamaikin, Y.-L. Li, E. Ridente, W. T. Chen, J.-S. Park, A. Y. Zhu, F. Capasso, M. Weidman, M. Schultze, F. Krausz, and N. Karpowicz, "Electric-field-resolved near infrared microscopy," submitted.
27. R. M. Koehl, S. Adachi, and K. A. Nelson, "Direct Visualization of Collective Wavepacket Dynamics," J. Phys. Chem. A **103**(49), 10260–10267 (1999).
28. Z. Jiang, X. G. Xu, and X.-C. Zhang, "Improvement of terahertz imaging with a dynamic subtraction technique," Appl. Opt. **39**(17), 2982–2987 (2000).
29. G. Gallot and D. Grischkowsky, "Electro-optic detection of terahertz radiation," J. Opt. Soc. Am. B **16**(8), 1204–1212 (1999).
30. N. Karpowicz, J. Dai, X. Lu, Y. Chen, M. Yamaguchi, H. Zhao, X.-C. Zhang, L. Zhang, C. Zhang, M. Price-Gallagher, C. Fletcher, O. Mamer, A. Lesimple, and K. Johnson, "Coherent heterodyne time-domain spectrometry covering the entire 'terahertz gap'," Appl. Phys. Lett. **92**(1), 011131 (2008).
31. C.-Y. Li, D. V. Seletskiy, Z. Yang, and M. Sheik-Bahae, "Broadband field-resolved terahertz detection via laser induced air plasma with controlled optical bias," Opt. Express **23**(9), 11436–11443 (2015).
32. M. Porer, J.-M. Ménard, and R. Huber, "Shot noise reduced terahertz detection via spectrally postfiltered electro-optic sampling," Opt. Lett. **39**(8), 2435–2438 (2014).
33. I. E. Ilyakov, G. K. Kitaeva, B. V. Shishkin, and R. A. Akhmedzhanov, "Terahertz time-domain electro-optic measurements by femtosecond laser pulses with an edge-cut spectrum," Opt. Lett. **41**(13), 2998–3001 (2016).
34. X. Wang, Y. Cui, W. Sun, J. Ye, and Y. Zhang, "Terahertz real-time imaging with balanced electro-optic detection," Opt. Commun. **283**(23), 4626–4632 (2010).
35. E. Ridente, M. Weidman, M. Mamaikin, C. Jakubeit, F. Krausz, and N. Karpowicz, "Hybrid phase-matching for optical parametric amplification of few-cycle infrared pulses," Optica **7**(9), 1093–1096 (2020).
36. S. Ahmed, J. Savolainen, and P. Hamm, "Detectivity enhancement in THz electrooptical sampling," Rev. Sci. Instrum. **85**(1), 013114 (2014).
37. J. A. Johnson, F. D. J. Brunner, S. Grübel, A. Ferrer, S. L. Johnson, and T. Feurer, "Distortion-free enhancement of terahertz signals measured by electro-optic sampling. II. Experiment," J. Opt. Soc. Am. B **31**(5), 1035–1040 (2014).
38. F. D. J. Brunner, J. A. Johnson, S. Grübel, A. Ferrer, S. L. Johnson, and T. Feurer, "Distortion-free enhancement of terahertz signals measured by electro-optic sampling. I. Theory," J. Opt. Soc. Am. B **31**(4), 904–910 (2014).
39. P. Krauspe, N. Banerji, and J. Réhault, "Effective detection of weak terahertz pulses in electro-optic sampling at kilohertz repetition rate," J. Opt. Soc. Am. B **37**(1), 127–132 (2020).
40. P. C. M. Planken, C. E. W. M. van Rijmenam, and R. N. Schouten, "Opto-electronic pulsed THz systems," Semicond. Sci. Technol. **20**(7), S121–S127 (2005).